

# Solid-phase steam-assisted synthesis of hydroxyapatite nanorods and nanoparticles

Shou Cang Shen · Leonard Chia · Wai Kiong Ng ·  
Yuan Cai Dong · Reginald B. H. Tan

Received: 1 February 2010/Accepted: 3 June 2010/Published online: 17 June 2010  
© Springer Science+Business Media, LLC 2010

**Abstract** This article reports a novel and facile solid-based steam-assisted conversion method for the synthesis of hydroxyapatite (HAP,  $\text{Ca}_{10}(\text{PO}_4)_6(\text{OH})_2$ ) nanorods and nanoparticles. After steam treatment at 180 °C for 20 h, the wet solid of brushite ( $\text{CaHPO}_4 \cdot 2\text{H}_2\text{O}$ ), which was precipitated from reaction between calcium nitrate [ $\text{Ca}(\text{NO}_3)_2$ ] and diammonium hydrogen phosphate [ $(\text{NH}_4)_2\text{HPO}_4$ ], was transformed to HAP nanorods with dimension of 100–300 nm in length and  $56 \pm 10$  nm in diameter through a solid–gas reaction. By the same steam treatment, the dried brushite was converted to nanoparticles of HAP with small aspect ratio and particle size of  $70 \pm 18$  nm. As compared with commercial HAP material, the nanostructured HAP materials exhibited superior sinterability in terms of density and hardness as well as excellent thermal stability. This simple, organic-free and cost-effective synthesis route with low reactant volume offers high potential for large-scale production of nanostructured HAP.

## Introduction

Due to its excellent biocompatibility and bioactivity [1–3], hydroxyapatite (HAP) has attracted great interest in the field of biomaterial research in recent years. The HAP material has excellent biological compatibility because it is the primary inorganic components of bone [4, 5]. HAP has been found to display osteoconductive properties [6, 7] and has been used in implant applications to stimulate bone regeneration [8]. Moreover, HAP has also been utilised as carriers for drug delivery and tissue engineering for bone regeneration [9–12]. Vallo et al. [13] found that the addition of up to 15 wt% of HAP to polymethylmethacrylate (PMMA) bone cement can improve the fracture toughness as well as flexural modulus of the bone cement. The particle size and the crystal structure of HAP have been found to affect its physical properties, such as fracture toughness and fracture strength [14]. It is therefore an important step to prepare fine and sinterable HAP nanorods similar to those found in natural bone for applications in bone tissue engineering.

The synthesis of nanostructured HAP has been intensively investigated to develop a suitable synthesis technique for large-scale production. These methods include mechanochemical synthesis [15], spark plasma sintering [16], combustion preparation [17] and high-temperature solid reaction [18]. In addition, various solution-based wet chemistry synthesis procedures, such as hydrothermal synthesis [19–21] and controlled precipitation from aqueous solutions in the presence of organic modifiers [22] or templates [23, 24], have been widely studied. Furthermore, electrochemical deposition [25], sol–gel procedures [26, 27] and emulsion techniques [28, 29] were also reported. The most commonly used solution-based chemical synthesis routes suffer low product yields as they are limited

S. C. Shen (✉) · L. Chia · W. K. Ng · Y. C. Dong ·  
R. B. H. Tan (✉)  
Institute of Chemical and Engineering Sciences, A\*STAR  
(Agency for Science, Technology and Research), 1 Pesek Road,  
Jurong Island 627833, Singapore  
e-mail: shen\_shoucang@ices.a-star.edu.sg

R. B. H. Tan  
e-mail: reginald\_tan@ices.a-star.edu.sg

R. B. H. Tan  
Department of Chemical and Biomolecular Engineering,  
The National University of Singapore, 4 Engineering Drive 4,  
Singapore 117576, Singapore

by reactor volume and reactant concentrations. It is desired to develop a cost-efficient process for the synthesis of HAP nanoparticles and nanorods with potential for large-scale production, as large-scale manufacturing of nanomaterials as affordable cost stands as the ultimate challenge for the application of nanomaterials and nanotechnology.

In this study, we have developed a simple and cost-effective solid-state steam treatment route to produce HAP nanorods and nanoparticles. This innovative solid-based synthesis route has inherited the advantages of solution-based hydrothermal synthesis, such as: (1) low synthesis temperature, (2) process with controlled nucleation during crystallization and (3) products with homogeneous composition as well as small particle size [30]. In addition, this solid-state reaction route ensures a low reactant volume and high throughput for subsequent scale-up production of nanocrystalline HAP. The process is distinguished by the simplicity of the apparatus for preparation and without the use of any surfactants or organic reagents. The as-synthesised HAP nanorods and nanoparticles were characterised by X-ray diffraction (XRD), Fourier transform infra-red (FTIR) spectroscopy, N<sub>2</sub> adsorption, hardness measurement, field emission scanning electron microscopy (FESEM) and transmission electron microscopy (TEM).

## Materials and synthesis methods

Typically, 15 mL of 0.5 M Ca(NO<sub>3</sub>)<sub>2</sub>·4H<sub>2</sub>O (Alfa Aesar) solution was added to 15 mL of 0.5 M (NH<sub>4</sub>)<sub>2</sub>HPO<sub>4</sub> (Alfa Aesar) solution to achieve the desired Ca<sup>2+</sup>/PO<sub>4</sub><sup>3-</sup> ratio of 1.0 for precipitation of di-calcium phosphate dihydrate (CaPO<sub>4</sub>·2H<sub>2</sub>O, Ca/P = 1:1) at 25 °C. The pH of the mixture was adjusted to 11.0 using aqueous ammonia solution (NH<sub>4</sub>OH, 25 wt%, Merck). The precipitate was recovered by filtration and then transferred to a 25 mL beaker, which was placed in an autoclave with a polytetrafluoroethylene (PTFE) liner. 5 mL of the ammonia solution was poured into the bottom of the PTFE cup and physically separated from the solid sample. The autoclave was then placed into an oven at 180 °C for 20 h. After the steam-assisted treatment, the resulting white solid was dispersed in water using ultrasound and recovered by centrifugation. The washing procedure was repeated twice. The obtained solid material was dried in an oven at 55 °C, and ground to a fine powder for characterisation. This sample of hydroxyapatite (Ca/P = 1.67:1) obtained by steam treatment of wet precipitate solid was denoted as HAP-A.

As a comparison, sample of HAP-B was prepared by a dry gel conversion procedure. Prior to steam treatment, the precipitate solid was dried at 60 °C for 24 h. The dried powder was treated under the same steaming conditions as HAP-A. More than 90% of HAP product yield could be

achieved by this solid-based steam treatment process. In addition, a commercial sample powder of HAP-C (Riedel-de Haën) was used as a comparison.

## Characterisation

X-ray diffraction measurements were performed on a D8-ADVANCE (BRUKER) X-ray diffractometer in steps of 0.02° using Cu K $\alpha$  radiation as the X-ray source. The framework vibration FTIR spectra was recorded on a TFS3000MX (BIO-RAD) infrared spectrophotometer at a resolution of 2 cm<sup>-1</sup>. The samples were thoroughly ground with KBr pellets before being pressed at 40 kN force to form a thin wafer. The morphology and size of the solid powder were observed with a FESEM (JEOL JSM-6700F) and TEM (TECNAI F20 (G<sup>2</sup>) (FEI)) operated at 125 kV. The specimens for HRTEM/TEM studies were prepared by suspending a solid sample in acetone with ultrasonic dispersion in a water bath.

Raman spectra were collected in a backscattering geometry by HR800 UV (JY Horiba) instrument equipped with a charge-coupled detector with visible laser light ( $\lambda = 514.5$  nm). The slits were adjusted to reach the resolution of 1 cm<sup>-1</sup>. The measurement was performed under microscope and the laser spot was estimated to be 1–2 μm in diameter.

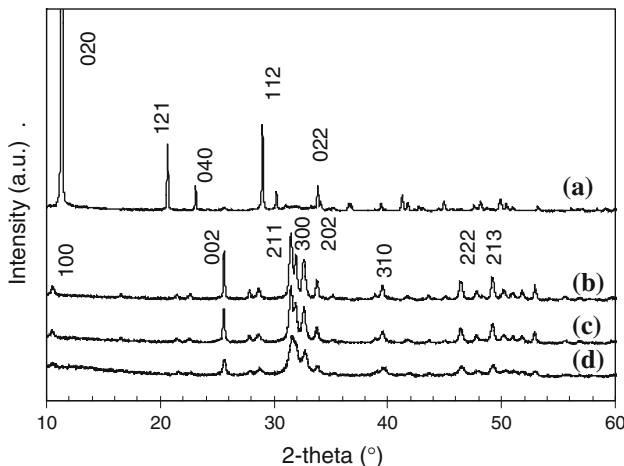
Sintering studies were conducted on samples of HAP pellets (10-mm diameter and 2-mm height) compacted at a pressure of 100 MPa, at various temperatures from 800 to 1300 °C for 12 h in air. The sintered pellets were subject to hardness, density, specific surface area and pore volume measurements. Density was measured by XS204 microbalance with density determination kit. According to Archimedes principle with water as the liquid medium, the density could be calculated using the formula:  $\rho = A/P \cdot \rho_0$  (g/cm<sup>3</sup>), where  $\rho$  is the density of the pellet,  $\rho_0$  is the density of the liquid,  $A$  is weight of the pellet, and  $P$  is the difference in weight of the pellet before and after immersion in the liquid. The hardness values were measured using a micro MMT-X3 hardness tester (MATSUZAWA, Japan) at a load of 200 g applied for 10 s on the smooth surface of the sintered pellets. The microhardness was calculated from the indentations using the formula:  $H_V = 1.854 L/d^2$ , where  $H_V$  is the Vickers hardness number,  $L$  is the applied load in kg and  $d$  is the diagonal length of the square indentation in mm.

The specific surface areas and pore volume of the HAP samples were measured using an Autosorb-6B gas adsorption analyzer (Quantachrome) at the temperature of -196 °C. Before measurement, each sample was vacuum dried at 200 °C for 24 h. The specific surface areas of the samples were determined from the linear portion of the Brumauer–Emmett–Teller (BET) plots.

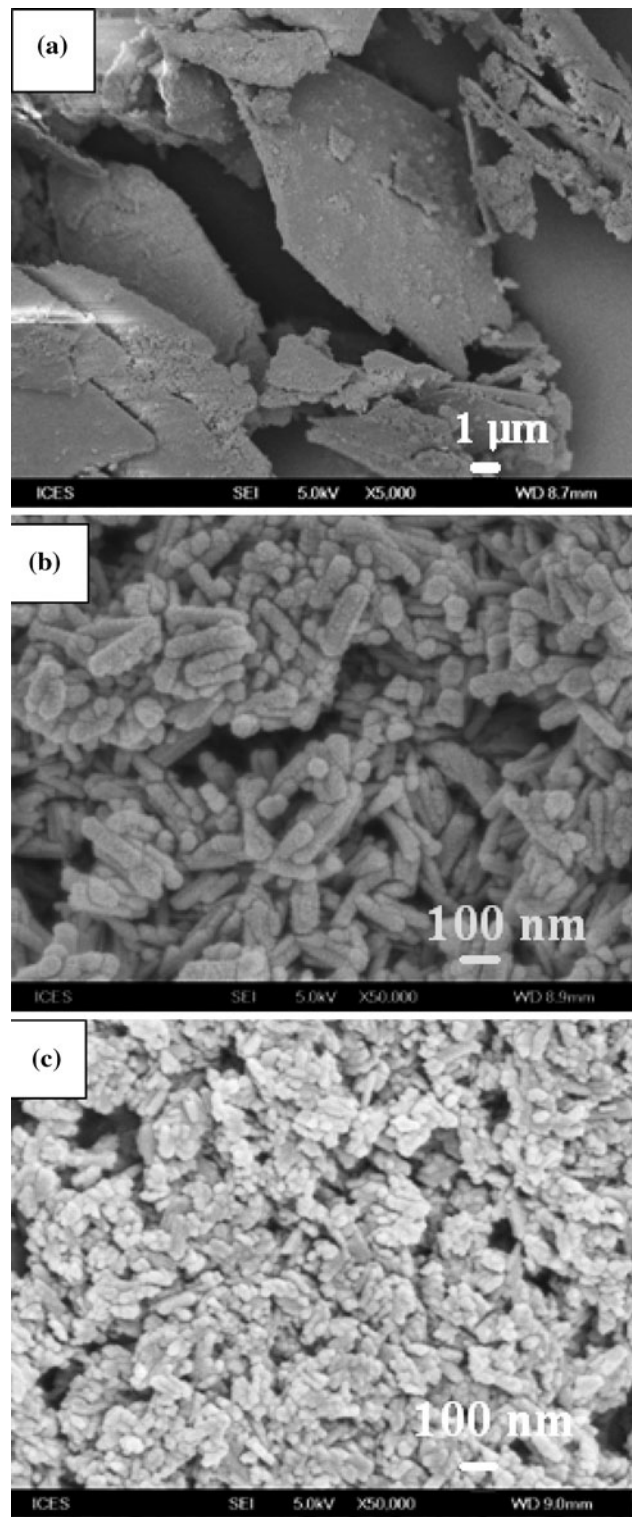
## Results and discussion

Figure 1 displays the XRD patterns of the solid precipitate before and after solid-state steam treatment. It can be seen that there was a crystal structure transformation by the steam treatment at 180 °C for 20 h. Before steam treatment, the brushite phase was the solid precipitate arising from the reaction between solutions of  $\text{Ca}(\text{NO}_3)_2$  and  $(\text{NH}_4)_2\text{HPO}_4$ . Although it was reported that brushite phase is stable at pH range of 2–6 [31], in this study, the precipitate obtained at pH 11 was filtrated and the crystal structure is well preserved. The brushite solid was crystalline and the XRD pattern was consistent with standard crystallite brushite (inorganic crystal structure database, ICSD, No 072-0713). The crystal structure was completely transformed after steam treatment using either wet or dried brushite as precursors. All XRD peaks can be indexed to HAP (ICSD, No. 009-0432). The XRD patterns of as-synthesized HAP-A and HAP-B are also in good agreement with commercial HAP-C material as shown in Fig. 1d. No characteristic peaks of impurities, such as calcium hydroxide and calcium phosphates are observed, implying that phase-pure HAP is obtained by the solid-state steam-assisted structural transformation. Though it has been reported that HAP could be synthesised by a solid-state reaction at high temperatures of 600–1250 °C [18], in this study, the utilisation of steam treatment has reduced the reaction temperature to 180 °C, which is a low typical temperature for solution-based hydrothermal synthesis.

The transformation in morphology from solid precipitate to the resultant HAP materials was revealed by FESEM as displayed in Fig. 2. Before steam treatment, the crystalline brushite is plate-shaped and ranged several tens of microns in size (Fig. 2a). After steam treatment at 180 °C for 20 h,



**Fig. 1** XRD patterns of (a) brushite obtained by precipitation, (b) HAP-A, (c) HAP-B and (d) commercial HAP-C



**Fig. 2** SEM images of **a** brushite obtained by precipitation, **b** HAP-A obtained by steam treatment of wet brushite and **c** HAP-B obtained by steam treatment of dried brushite

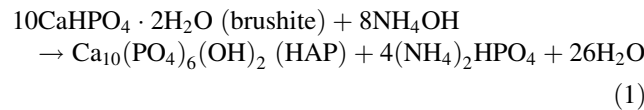
the micron-sized plate-shaped crystal was converted to a nano-structured material under the solid-based hydrothermal conditions. As shown in Fig. 2b, nanorods of HAP-A

obtained by steam treatment of wet precipitate exhibited dimension of  $56 \pm 10$  nm in diameter and 100–300 nm in length with aspect ratios in the range of 2–5. The morphology of the resulting nanocrystalline HAP was found to be affected by the moisture content of the raw brushite solid. When the brushite raw material was dried at 60 °C prior to the steam treatment, smaller nanoparticles of HAP-B were harvested after the same steam treatment as HAP-A. The particle size of HAP-B obtained by a dry-gel conversion route is smaller than 100 nm ( $70 \pm 18$  nm) with a low aspect ratio.

Figure 3 exhibits the FTIR spectra of the brushite precipitate and the samples of HAP-A and HAP-B obtained by solid-state steam treatment of wet and dried brushite. At the high-frequency region of 3000–4000 cm<sup>-1</sup>, the brushite solid exhibits four characteristic bands at 3171, 3323, 3495 and 3549 cm<sup>-1</sup>, which are attributed to the presence of hydrate water with the stretching and bending vibrations of the two types of water molecules. The doublet below 3400 cm<sup>-1</sup> is assigned to the antisymmetric and symmetric stretching vibrations of the water molecules that are more strongly hydrogen bonded, which, at higher frequencies is attributed to the vibrations of loosely hydrogen bonded water molecules [32]. After steam treatment of either wet or dried brushite, crystallized hydroxyapatite exhibits a different FTIR spectrum. A sharp peak at 3573 cm<sup>-1</sup> is observed and it is assigned to the stretching vibration of the lattice OH<sup>-</sup> ions. The absorbance bands due to the vibrations of hydrogen-bonded water disappeared. Similarly, the strong band at 1652 cm<sup>-1</sup> due to water molecules in the spectrum of brushite became much weakened after being converted to hydroxyapatite with physically adsorbed water. At the low-frequency region, brushite crystal

exhibited three strong resolved bands at 1137, 1063 and 988 cm<sup>-1</sup>, attributed to PO stretches localised mainly in the PO<sub>3</sub> fragment [32]. After being converted to HAP, all samples show typical HAP apatite phosphate modes near 1095, 1040 and 964 cm<sup>-1</sup> which is characteristic of the phosphate stretching vibration. Bands observed at 601, 563 and 480 cm<sup>-1</sup> are due to the phosphate bending vibration [33]. A medium sharp peak at 632 cm<sup>-1</sup> is assigned to the OH group of HAP. The broad bands at 3467 and 1657 cm<sup>-1</sup> are due to moisture physically adsorbed on HAP. Due to contact with ambient carbon dioxide (CO<sub>2</sub>) during processing, the formation of carbonate ions in the resultant HAP exhibited weak IR bands at 1480 and 1428 cm<sup>-1</sup>. The result of FTIR analysis further confirms that the as-synthesised powders are pure HAP [22, 34].

Figure 4 displays the TEM images of HAP-A and HAP-B obtained by steam treatment of wet and dried brushite precipitates. The as-synthesised HAP-A is well-dispersed and exhibits a rod-like shape. HRTEM analysis (Fig. 4c, d) of a single rod indicates that the obtained HAP nanorod is highly crystalline. Figure 4c displays a HRTEM image taken along the lateral direction of a HAP nanorod with a lattice about 0.35 nm, which is assigned to the (002) planes of the hexagonal crystal structure of HAP. The result implies that HAP nanorods are formed through preferential growth along the *c*-axis by (002) planes stacking. Figure 4d exhibits a HRTEM image taken at the tip of the HAP nanorod. The terminal end by (002) planes provides further evidence of the crystal growth along *c*-axis. In addition, the lattice spacing of about 2.8 Å corresponding to the (211) planes also clearly indicated that the nanorods of HAP are highly crystalline, which is in good agreement with XRD data. It has been reported that crystalline nanorods of HAP can be synthesised by hydrothermal treatment in the liquid-phase [19, 34]. In this study, the nanorods of HAP were synthesised through a solid-phase hydrothermal transformation instead of a solution-based reaction. The steam treatment resulted in the transformation in crystal structure and morphology of the wet brushite precipitate to HAP nanorods. Steam initiated a local hydrothermal condition for reaction between the brushite precipitate and ammonium hydroxide to form the thermodynamically stable HAP:



The water of crystallization in brushite was released inside the closed autoclave during the formation of HAP, enabling the local hydrothermal condition to be maintained for continued reaction and crystallisation of HAP with the assistance of steam. The preferential direction of HAP crystal growth in this solid phase exhibited similar growth

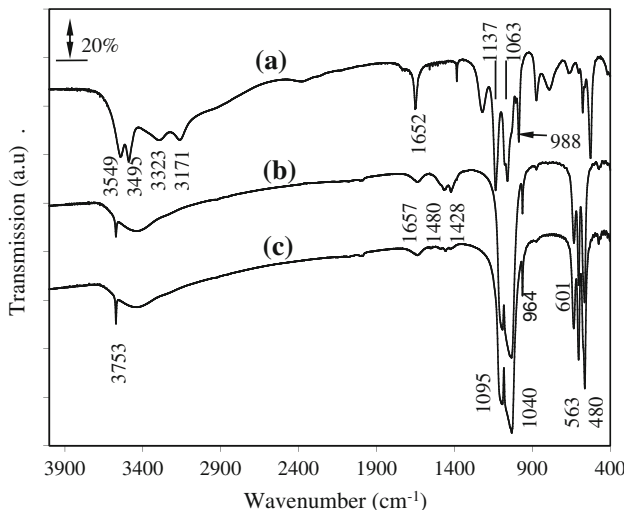


**Fig. 3** FTIR spectra of (a) brushite, (b) HAP-A and (c) HAP-B

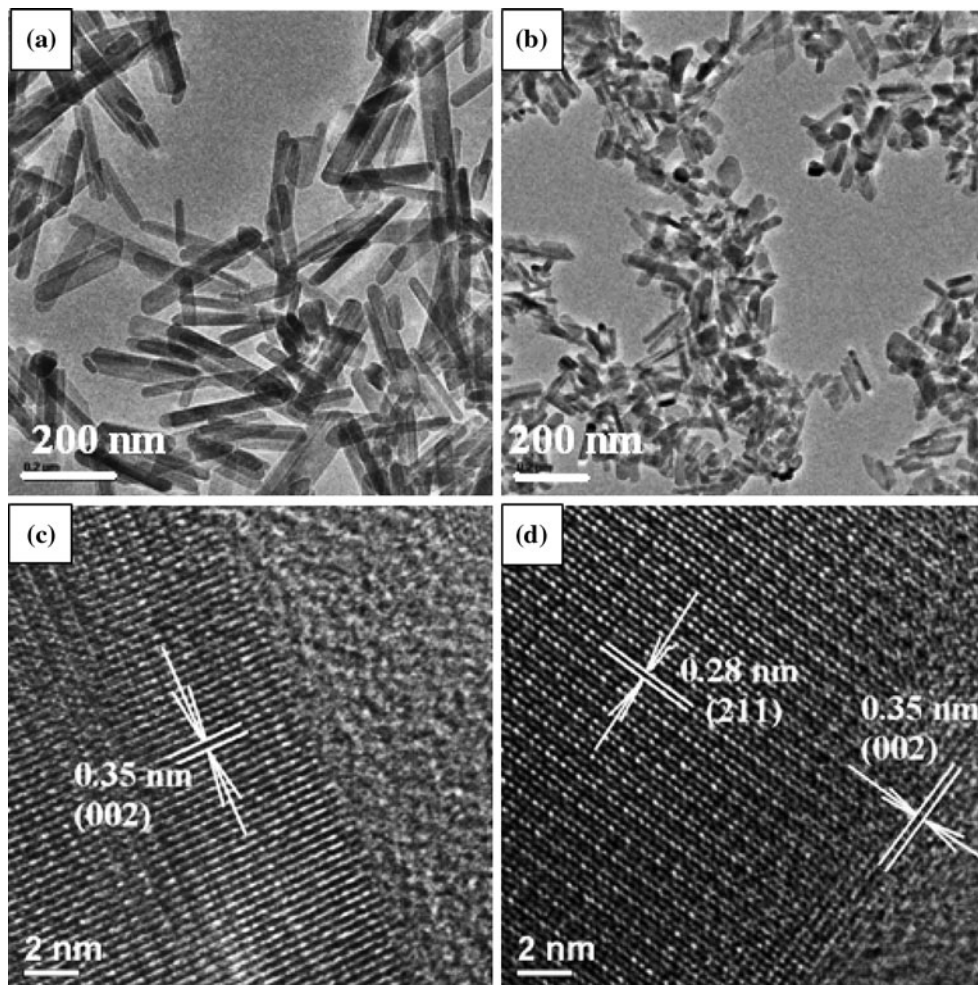


**Fig. 4** TEM images of **a** HAP-A, **b** HAP-B and HRTEM images of a single nanorod at **(c)** lateral and **(d)** tip of HAP-A

habit in solution-based syntheses [35] and led to the formation of nanorods. The morphology of nanocrystalline HAP was found to depend on the water content of raw brushite before steam treatment. When the dried brushite was steam-treated under the same conditions, smaller nanoparticles with low aspect ratio were obtained as shown in Fig. 4b. Under steam treatment, dried brushite could be recrystallized to HAP through nucleation and crystal growth. However, due to the lack of sufficient moisture inside the solid phase, the mobility of the nucleus is limited and the transport of materials to support the crystal growth of HAP along the preferential direction is limited under the dry gel steam condition. Consequently, smaller nanoparticles of HAP were formed through a dry-gel conversion route.

Results of Raman measurements indicated in Fig. 5 support the structure transformation under steam treatment. Brushite exhibited characteristic peak at  $876\text{ cm}^{-1}$  due to mode  $v_1$  vibration of  $\text{HPO}_4^{2-}$  and at  $988\text{ cm}^{-1}$  to the mode  $v_1$  of  $\text{PO}_4^{3-}$  [36]. OH stretching of water molecules in brushite gave broad bands at  $3467$  and  $3535\text{ cm}^{-1}$ . After

steam treatment, the Raman spectrum was completely changed as the crystal structure was transformed to HAP. Both samples of HAP-A and HAP-B exhibit the very intensive and characteristic peak at  $952\text{ cm}^{-1}$ , which is attributed to the mode  $v_1$   $\text{PO}_4$  symmetric stretching of HAP

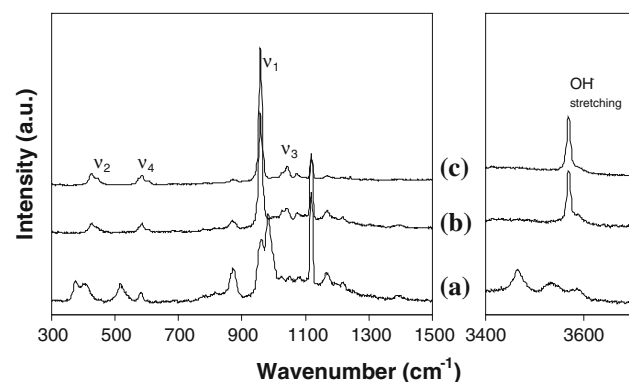


**Fig. 5** Raman spectra of **(a)** solid brushite, **(b)** HAP-A and **(c)** HAP-B

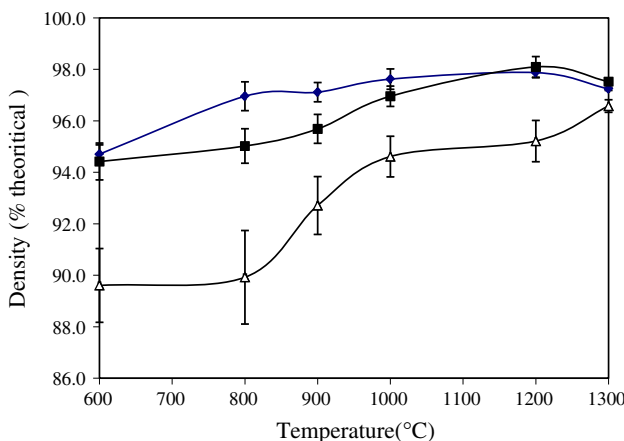


**Fig. 6** Variation in relative density of HAP pellets with sintering temperatures (three samples were used for each measurement,  $n = 3$ )

[37]. The two weak peaks at  $433$  and  $588\text{ cm}^{-1}$  are regarded as  $\nu_2$  and  $\nu_4$   $\text{PO}_4$  modes, respectively. The vibration of  $\nu_3$   $\text{PO}_4$  modes contributed to the weak bands in the region of  $1020$ – $1077\text{ cm}^{-1}$ .  $\nu_1$   $\text{CO}_3$  mode results in a very weak peak at  $1080\text{ cm}^{-1}$  [38]. At the high-frequency region, a sharp band at  $3570\text{ cm}^{-1}$  is ascribed to stretching vibration of ionic OH groups of HAP, which did not appear in the brushite spectrum.

Figure 6 displays the variation in density of HAP pellets as a function of sintering temperature. After thermal treatment at  $600\text{ }^\circ\text{C}$  for  $12\text{ h}$ , both nanostructured HAP-A and HAP-B have reached  $94.4\%$  of the theoretical density of HAP ( $3.156\text{ g/cm}^3$ , JCPDS 9-432), whereas HAP-C has reached a relative density of  $89.6\%$  only. With an increase in sintering temperature, all samples showed an increase in relative density. It is noticed that nanocrystalline HAP-A and HAP-B exhibited a higher relative density than that of commercial HAP-C across the temperature range tested. HAP-A and HAP-B reached a maximum relative density ( $98\%$  of the theoretical density) at  $1200\text{ }^\circ\text{C}$ , which has been found to be comparable with the reported value for sintered pellets of nanocrystalline HAP prepared by a co-precipitation process [39]. At this temperature, HAP-C reached  $95.2\%$  of the theoretical density of HAP.

The sinterability of nanocrystalline HAP particles has also been evaluated by  $\text{N}_2$  adsorption from  $600$  to  $1,200\text{ }^\circ\text{C}$  and the results are compared with HAP-C. As shown in Table 1, the freshly as-synthesized nanorods of HAP-A has a specific surface area of  $46.1\text{ m}^2/\text{g}$ . HAP-B exhibits a higher specific surface area of  $72\text{ m}^2/\text{g}$  due to its smaller particle size. The specific surface area of freshly as-synthesized HAP nanorods and nanoparticles through steam-assisted solid phase synthesis procedure is comparable to nanocrystalline HAP reported by solution-based methods [21, 39]. With an increase in sintering temperatures, the

specific surface area of thermal-treated HAP shrank sharply. Both samples of HAP-A and HAP-B exhibited lower specific surface areas and pore volumes than HAP-C at all thermal treatment temperatures. After being sintered at  $1200\text{ }^\circ\text{C}$  for  $12\text{ h}$ , the specific surface areas of HAP-A and HAP-B decreased to such a low level that is not measurable by Autosorber-6B, whereas HAP-C had a specific surface area of  $0.24\text{ m}^2/\text{g}$  and pore volume of  $0.59 \times 10^{-2}\text{ cc/g}$ .

Figure 7 displays the FESEM images of thermal-treated HAP pellets after being sintered at  $1200\text{ }^\circ\text{C}$  for  $12\text{ h}$  as compared with HAP-C. The images were taken from the outer surfaces of pellets and their fractured surfaces. It is clearly seen that HAP-A and HAP-B exhibited much better sinterability than HAP-C. The nanocrystalline HAP particles have been well sintered to form a dense solid. No observable porous structure was observed in HAP-A and HAP-B both on the outer surface and on the fractured cross-section surface after thermal treatment at  $1200\text{ }^\circ\text{C}$ . In comparison, HAP-C pellet still shows a large number of observable pores on either at the outer surface or at the cross-section. These images tally well with the earlier measured higher density and lower surface areas of HAP-A and HAP-B pellets as compared to HAP-C after being thermal sintered.

The variation in hardness values of HAP pellets at different sintering temperatures is shown in Fig. 8. After being sintered at  $800\text{ }^\circ\text{C}$  for  $12\text{ h}$ , all samples exhibit a low hardness value of  $\sim 50\text{ Hv}$ . The trend of hardness variation with temperature is similar to the change in relative density. With an increase in sintering temperature, the hardness of HAP-A increases and reaches its highest value of  $608\text{ Hv}$  at  $1200\text{ }^\circ\text{C}$ . HAP-B has a maximum hardness of  $580\text{ Hv}$  at  $1100\text{ }^\circ\text{C}$  (Table 2). Raising sintering temperature from  $1000$  to  $1100\text{ }^\circ\text{C}$  resulted in significant increase in the hardness of sintered HAP pellets. However, HAP-C has a much lower hardness value than HAP-A and HAP-B at this temperature region. The results indicate that nanostructured HAP possess high sinterability to form highly condensed microcrystalline materials.

Thermal stability of the HAP powder is important for the potential application in the coating of metallic implants which usually involves a post-coating heat treatment at high temperature [40]. To examine the thermal stability of the HAP, a small amount of the sample was heated up to  $1300\text{ }^\circ\text{C}$  for  $12\text{ h}$  and powder XRD patterns were recorded accordingly. Figure 9 displays XRD patterns of HAP-A and HAP-B after the thermal treatment at different temperatures. The results indicated that HAP represented a major phase up to  $1300\text{ }^\circ\text{C}$  and minor diffraction peaks assigned to tricalcium phosphate ( $\beta$ -TCP) were observed. In contrast, it has been found that HAP prepared by using egg-shell as a calcium source [41] was decomposed to calcium oxide after being sintered at  $1250\text{ }^\circ\text{C}$  and synthesized by co-precipitation was decomposed to  $\beta$ -TCP

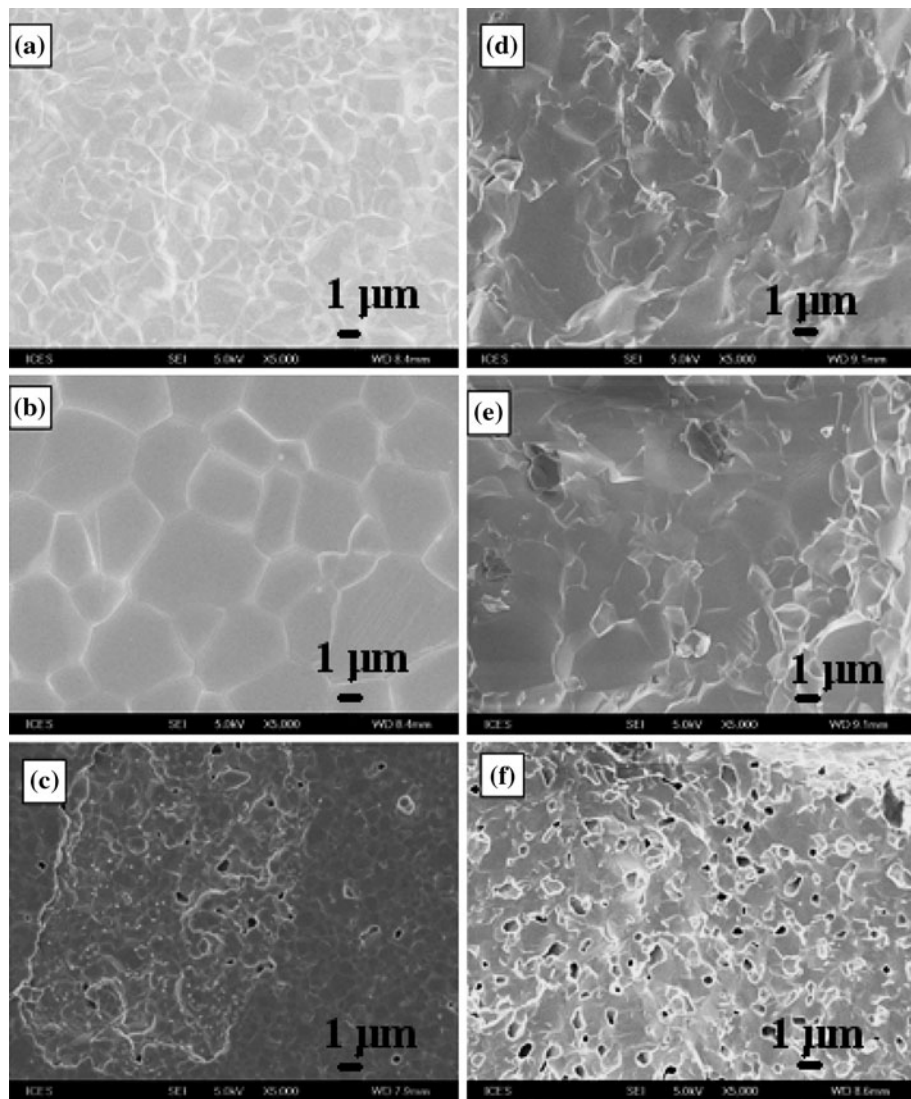
**Table 1** Specific surface areas and total pore volume of HAP samples after being sintered at different temperatures for 12 h

	As-synthesized <sup>a</sup>	600 °C	800 °C	1000 °C	1200 °C
Specific surface areas (m <sup>2</sup> /g)					
HAP-A	46.1	25.5	7.3	0.8	<sup>b</sup>
HAP-B	72.0	32.3	8.3	0.4	<sup>b</sup>
HAP-C	80.3	35.3	11.7	1.74	0.24
Total pore volume (cc/g)					
HAP-A	0.15	$5.1 \times 10^{-2}$	$1.3 \times 10^{-2}$	$0.45 \times 10^{-2}$	<sup>b</sup>
HAP-B	0.28	$6.9 \times 10^{-2}$	$1.6 \times 10^{-2}$	$0.59 \times 10^{-2}$	<sup>b</sup>
HAP-C	0.23	$8.1 \times 10^{-2}$	$2.0 \times 10^{-2}$	$0.68 \times 10^{-2}$	$0.59 \times 10^{-2}$

<sup>a</sup> As-synthesized sample was measured in powder form

<sup>b</sup> Below measurement limit of surface area and pore volume measurement by Autosorb-6B

**Fig. 7** SEM surface image of **a** HAP-A, **b** HAP-B, **c** HAP-C and fractured surface of **d** HAP-A, **e** HAP-B, **f** HAP-C after thermal treatment at 1200 °C for 12 h



as a major phase when sintered at 1300 °C [39]. In this study, the HAP materials obtained by a solid-based steam treatment process exhibited thermal stability, while they

also showed the superior sinterability at high temperatures. It should be noted that this synthesis route is free of organic reagents, whereas organic modifiers were reported to

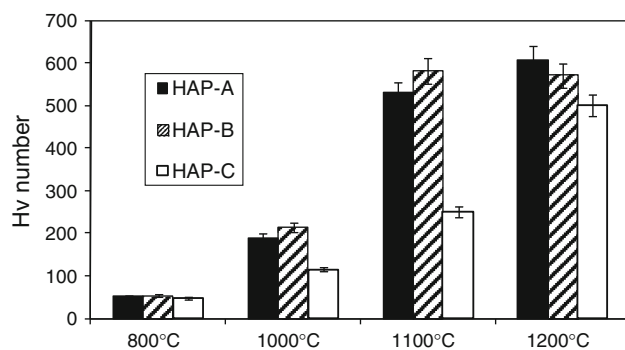


**Fig. 8** Hardness of HAP pellets at different sintering temperatures (three samples were used for each measurement,  $n = 3$ )

control the morphology of HAP nanorods [22]. The formation of nanorods in this solid phase synthesis route is also free of the soft surfactant of cetyltrimethylammonium bromide (CTAB), which was used for solution-based syntheses of HAP nanorods [34, 42]. This simple organic-free, cost-effective synthesis route with low reactant volume offers potential for large-scale production of high-quality nanostructured HAP with excellent sinterability and thermal stability.

## Conclusions

Nanoparticles and nanorods of HAP have been synthesised by an innovative solid-state steam treatment through solid-gas reaction. After the steam treatment at 180 °C for 20 h, solid brushite was re-crystallised as nanostructured HAP with controlled morphology. When wet brushite was treated, nanorods of HAP with aspect ratios of 2–5 were obtained. As a comparison, the treatment of dried brushite led to formation of nanoparticles with low aspect ratios. This method possesses advantages in terms of process simplicity and avoiding the use of any surfactants, solvents or seeds while producing HAP nanorods with high purity and yields. The results of XRD, SEM, surface area and

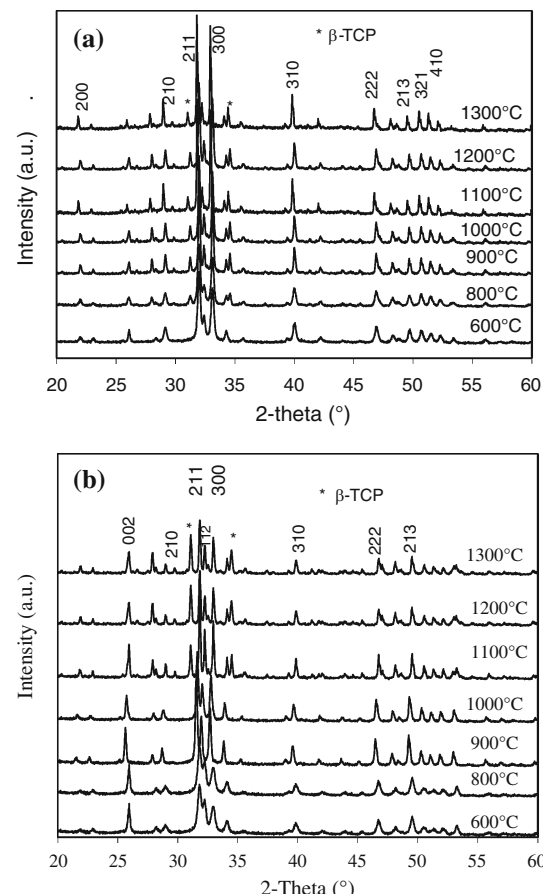


**Fig. 9** XRD patterns of **a** HAP-A and **b** HAP-B after thermal treatment at different temperatures for 12 h

hardness measurements indicated that the nano-structured HAP materials exhibited excellent sinterability. In addition, the results demonstrated that this low reactant volume solid-phase synthesis route could potentially be used for low-cost fabrication of other nano-structured materials at a large scale instead of conventional solution-based hydrothermal synthesis.

**Table 2** Density and hardness of HAP samples after being sintered at different temperature for 12 h

	600 °C	800 °C	900 °C	1000 °C	1100 °C	1200 °C	1300 °C
Density (g/cm <sup>3</sup> )							
HAP-A	2.989	3.060	3.065	3.081	—	3.089	3.069
HAP-B	2.980	2.999	3.020	3.060	—	3.096	3.078
HAP-C	2.828	2.838	2.926	2.986	—	3.005	3.048
Hardness (Hv number)							
HAP-A	51.2	—	—	189.0	529.1	608.5	—
HAP-B	53.6	—	—	213.6	580.7	571.0	—
HAP-C	48.2	—	—	115.3	250.5	500.1	—

**Acknowledgement** This work was supported by the Science and Engineering Research Council of A\*STAR (Agency for Science, Technology and Research), Singapore.

## References

1. Cao W, Hench LL (1996) *Ceram Int* 22:493
2. Hench LL (1998) *J Am Ceram Soc* 81:1705
3. Kaneko T, Ogomi D, Mitsugi R, Serizawa T, Akashi M (2004) *Chem Mater* 16:5596
4. Huang J, Best SM, Bonfield W, Brooks RA, Rushton N, Jayasinghe SN, Edirisinghe MJ (2004) *J Mater Sci Mater Med* 15:441
5. Nemoto R, Nakamura S, Isobe T, Senna M (2001) *J Sol-Gel Sci Technol* 21:7
6. Chen QZ, Wong CT, Lu WW, Cheung KMC, Leong JCY, Luk KDK (2004) *Biomater* 25:4243
7. Okumura M, Ohgushi H, Dohi Y, Katuda T, Tamai S, Koerten HK, Tabata S (1997) *J Biomed Mater Res A* 37:122
8. Jarcho M (1981) *Clin Orthop Relat Res* 157:259
9. Yao J, Tjandra W, Chen YZ, Tam KC, Ma J, Soh B (2003) *J Mater Chem* 13:3053
10. Saito T, Akeuchi R, Hirakawa K, Nagata N, Yoshida T, Koshino T, Okuda K, Takeda M, Hori T (2002) *J Biomed Mater Res: Appl Biomater* 63:245
11. Shinto Y, Uchida A, Korkusuz F, Araki N, Ono K (1992) *J Bone Joint Surg* 74B:600
12. Matsumoto T, Okazaki M, Nakahira A, Sasaki J, Egusa H, Sohmura T (2007) *Curr Med Chem* 14:2726
13. Vallo CI, Montemartini PE, Fanovich MA, Porto-López JM, Cuadrado TR (1998) *J Biomed Mater Res A* 48:150
14. Riman RE, Suchanek WL, Byrappa K, Chen CW, Shuk P, Oakes CS (2002) *Solid State Ionics* 151:393
15. Suchanek WL, Shuk P, Byrappa K, Rimman RE, Huisen KST, Janas VF (2002) *Biomater* 23:699
16. Guo XY, Xiao P, Liu J, Shen ZJ (2005) *J Am Ceramic Soc* 88:1026
17. Tas AC (2000) *J Eur Ceramic Soc* 20:2389
18. Ramachandra R, Roopa HN, Kannan TS (1997) *J Mater Sci Mater Med* 8:511
19. Neira IS, Guitián F, Taniguchi T, Watanabe T, Yoshimura M (2008) *J Mater Sci* 43:2171. doi:[10.1007/s10853-007-2032-9](https://doi.org/10.1007/s10853-007-2032-9)
20. Zhang X, Vecchio KS (2007) *J Crys Growth* 38:133
21. Chen JD, Wang YJ, Wei K, Zhang SH, Shi XT (2007) *Biomater* 28:2275
22. Wang AL, Liu D, Yin H, Wu H, Wada Y, Ren M, Jiang, Cheng X, Xu Y (2007) *Mater Sci Eng C* 27:865
23. Banerjee A, Bandyopadhyay A, Bose S (2007) *Mater Sci Eng C* 27:729
24. Wu YJ, Bose S (2005) *Langmuir* 21:3232
25. Lu X, Zhao Z, Leng Y (2005) *J Cryst Growth* 284:506
26. Bose S, Saha SK (2003) *J Am Ceram Soc* 86:1055
27. Bigi A, Boanini E, Rubini K (2004) *J Solid State Chem* 177:3092
28. Bose S, Saha SK (2003) *Chem Mater* 15:4464
29. Sun YX, Guo GS, Wang ZH, Guo HY (2006) *Ceramics Int* 32:951
30. Segal D (1989) Chemical synthesis of advanced ceramic materials. Cambridge University Press, Cambridge
31. Dorozhkin SV (2010) *Acta Biomater* 6:715
32. Trpkovska M, Soptrajanov B, Malkov P (1999) *J Mol Struct* 480–481:661
33. Fowler BO (1974) *Inorg Chem* 13:207
34. Lin K, Chang J, Cheng R, Ruan M (2007) *Mater Lett* 61:1683
35. Eda K, Uno Y, Nagai N, Sotani N, Chen C, Whittingham MS (2006) *J Solid State Chem* 179:1453
36. Penel G, Leroy N, Landuyt PV, Flauter B, Hardouin P, Lemaitre J, Leroy G (1999) *Bone* 25:81S
37. Silva CC, Sombra ASB (2004) *J Phys Chem Solids* 65:1031
38. Kazanci M, Fratzl P, Klaushofer K, Paschalis EP (2006) *Calcif Tissue Int* 79:35
39. Kong LB, Ma J, Boey F (2002) *J Mater Sci* 37:1131. doi:[10.1023/A:1014355103125](https://doi.org/10.1023/A:1014355103125)
40. Mavis B, AC TAS (2000) *J Am Ceram Soc* 83:989
41. Krishna DSR, Siddharthan A, Seshadri SK, Kumar TSS (2007) *J Mater Sci Mater Med* 18:1735
42. Sun Y, Guo G, Tao D, Wang Z (2007) *J Phy Chem Solids* 68:373